

Quantum error correction of a qubit encoded in grid states of an oscillator

<https://doi.org/10.1038/s41586-020-2603-3>

Received: 8 November 2019

Accepted: 12 June 2020

Published online: 19 August 2020

 Check for updates

P. Campagne-Ibarcq^{1,3,6}✉, A. Eickbusch^{1,6}, S. Touzard^{1,4,6}✉, E. Zalys-Geller¹, N. E. Frattini¹, V. V. Sivak¹, P. Reinhold¹, S. Puri¹, S. Shankar^{1,5}, R. J. Schoelkopf¹, L. Frunzio¹, M. Mirrahimi² & M. H. Devoret^{1,3}✉

The accuracy of logical operations on quantum bits (qubits) must be improved for quantum computers to outperform classical ones in useful tasks. One method to achieve this is quantum error correction (QEC), which prevents noise in the underlying system from causing logical errors. This approach derives from the reasonable assumption that noise is local, that is, it does not act in a coordinated way on different parts of the physical system. Therefore, if a logical qubit is encoded non-locally, we can—for a limited time—detect and correct noise-induced evolution before it corrupts the encoded information¹. In 2001, Gottesman, Kitaev and Preskill (GKP) proposed a hardware-efficient instance of such a non-local qubit: a superposition of position eigenstates that forms grid states of a single oscillator². However, the implementation of measurements that reveal this noise-induced evolution of the oscillator while preserving the encoded information^{3–7} has proved to be experimentally challenging, and the only realization reported so far relied on post-selection^{8,9}, which is incompatible with QEC. Here we experimentally prepare square and hexagonal GKP code states through a feedback protocol that incorporates non-destructive measurements that are implemented with a superconducting microwave cavity having the role of the oscillator. We demonstrate QEC of an encoded qubit with suppression of all logical errors, in quantitative agreement with a theoretical estimate based on the measured imperfections of the experiment. Our protocol is applicable to other continuous-variable systems and, in contrast to previous implementations of QEC^{10–14}, can mitigate all logical errors generated by a wide variety of noise processes and facilitate fault-tolerant quantum computation.

The qubit encoding proposed by GKP is based on grid patterns in phase space, which only emerge by interfering periodically spaced position eigenstates with adequate phase relationships, as shown in Fig. 1. The resulting ‘grid-state’ code belongs to the class of stabilizer codes. In the stabilizer formalism of QEC, the measurement of chosen operators—the stabilizers—reveals unambiguously the action of undesired noise without disturbing the state of the logical qubit. As a consequence of this latter condition, the stabilizers must commute with all observables of the logical qubit, which are combinations of the logical Pauli operators. For the grid-state code, these operators are phase-space displacements, defined as $\mathbf{D}(\beta) = \exp(-i\text{Re}(\beta)\mathbf{p} + i\text{Im}(\beta)\mathbf{q})$, where \mathbf{q} and \mathbf{p} are the conjugated position and momentum operators, such that $[\mathbf{q}, \mathbf{p}] = i$. For example, the stabilizers of the canonical square grid-state code are $\mathbf{S}_a = \mathbf{D}(a = 2\sqrt{\pi})$ and $\mathbf{S}_b = \mathbf{D}(b = 2i\sqrt{\pi})$, and the Pauli operators are $\mathbf{X} = \mathbf{D}(a/2)$, $\mathbf{Z} = \mathbf{D}(b/2)$ and $\mathbf{Y} = \mathbf{D}((a+b)/2)$. The phase of the stabilizers encodes no information about the logical qubit, but reveals the momentum shifts modulo $2\pi/|a|$ and the position shifts modulo $2\pi/|b|$. Thus, shifts that are smaller than a quarter of a grid period are

unambiguously identified and can be corrected. Because usual decoherence processes, such as photon relaxation^{15,16}, pure dephasing and spurious nonlinearities, result in a continuous evolution of the quasi-probability distribution in phase space^{2,17}, shifts of order a, b do not occur instantaneously. Therefore, if the stabilizers are measured frequently enough, noise-induced shifts can be detected and corrected, which inhibits all logical errors.

However, in contrast to this description, which is based on ideal position eigenstates, physically realizable code states do not extend infinitely in phase space; they are superpositions of periodically spaced squeezed states of width σ , with a Gaussian overall envelope of width $\Delta = 1/(2\sigma)$ (see Fig. 1a). These states are still approximate eigenstates of the stabilizers, such that $|\langle \mathbf{S}_{a,b} \rangle| \approx 1$. Any pair of orthogonal logical states are shifted from one to the other in phase space (for example, by $a/2$ for $|\pm Z_L\rangle$ and $b/2$ for $|\pm X_L\rangle$). For sufficient squeezing, their supports do not considerably overlap, the logical qubit is well defined, and a QEC protocol can be directly adapted from the ideal case.

¹Department of Applied Physics, Yale University, New Haven, CT, USA. ²Quantic Team, INRIA Paris, Paris, France. ³Present address: Quantic Team, INRIA Paris, Paris, France. ⁴Present address: Centre for Quantum Technologies, National University of Singapore, Singapore, Singapore. ⁵Present address: Department of Electrical and Computer Engineering, University of Texas, Austin, TX, USA. ⁶These authors contributed equally: P. Campagne-Ibarcq, A. Eickbusch, S. Touzard. ✉e-mail: philippe.campagne-ibarcq@inria.fr; steven.touzard@nus.edu.sg; michel.devoret@yale.edu

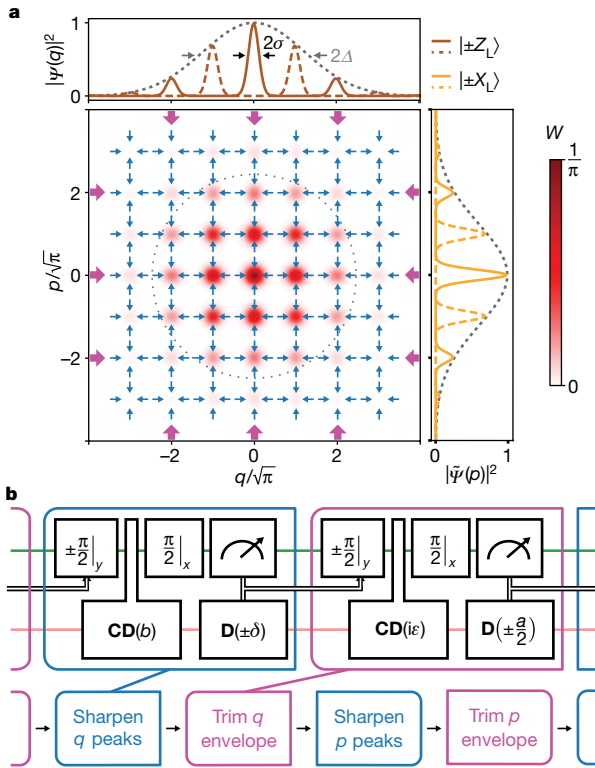


Fig. 1 | Quantum error correction protocol. **a**, Simulated Wigner function of the fully mixed logical state in a code defined by a width of $\sigma = 0.25$ for the peaks and of $\Delta = 1/(2\sigma) = 2$ for the normalizing envelope. Our QEC protocol prevents the squeezed peaks from spreading (blue arrows) and the overall envelope from extending (purple arrows). The side panels present the probability distributions of the $|\pm X_L\rangle$ and $|\pm Z_L\rangle$ states along each quadrature, which retain disjoint supports along q or p under stabilization. **b**, The full QEC protocol interleaves two peak-sharpening rounds and two envelope-trimming rounds to prevent spreading of the grid-state peaks and envelope in phase space (blue and purple arrows in **a**, respectively). In each round, a conditional displacement entangles the transmon (green line) and the storage oscillator (pink line). A subsequent measurement of the transmon controls the sign of a feedback shift of the oscillator and of a $\pi/2$ rotation resetting the transmon (bold black arrows). The peak-sharpening shift $\delta \approx 0.2$ maximizes the stabilizer value in the steady state, and the envelope-trimming conditional displacement of $\varepsilon \approx 0.2$ sets the width of the grid-state envelope (see Supplementary Figs. 10, 11), which is optimal given the experimental constraints.

Measurement of displacement operators

The expectation value of displacement operators $\mathbf{D}(\beta)$, such as the stabilizers and Pauli operators of the GKP code, are periodic functions of the generalized quadrature, $\mathbf{r} = -\text{Re}(\beta)\mathbf{p} + i\text{Im}(\beta)\mathbf{q}$. We measure these ‘modular variables’^{8,18,19} by effectively coupling the quadrature of an oscillator to the Pauli operator σ_z of an ancillary physical qubit. In our experiment, the oscillator is the fundamental mode of a reentrant coaxial microwave cavity made from bulk aluminium²⁰, which we call the storage mode, and the ancillary physical qubit is a transmon (see Supplementary Fig. 1). The storage mode has a single-photon lifetime of $T_s = 245 \mu\text{s}$ (see Supplementary Fig. 5), and the transmon has energy and coherence lifetimes of $T_1 = 50 \mu\text{s}$ and $T_{2E} = 60 \mu\text{s}$ —measured with an echo sequence—and can be non-destructively measured in 700 ns via an ancillary low-quality-factor resonator (see Supplementary Table 1 and Supplementary Fig. 3). Interestingly, the desired coupling $\mathbf{r} \otimes \sigma_z$ between the storage mode and the transmon can be effectively activated with microwave drives in the presence of the naturally present dispersive interaction²¹, even with arbitrarily weak interaction strength.

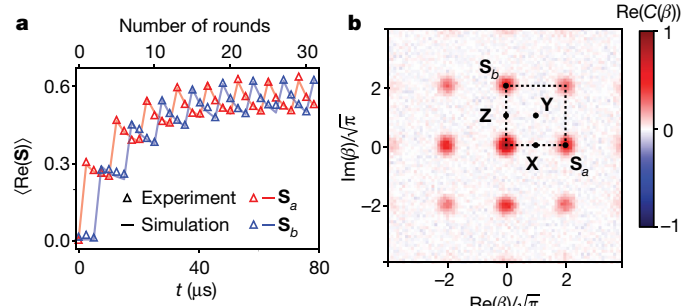


Fig. 2 | Square code in the steady state of the QEC protocol. **a**, Measured average value of the real part of the code stabilizers when turning on the QEC protocol from the vacuum state. Each stabilizer oscillates over a four-round period as a result of the periodicity of the QEC protocol, and the steady state is reached in about 20 rounds. **b**, Real part of the measured characteristic function of the storage mode in the steady state (after 200 rounds). Points corresponding to stabilizers and Pauli operators are indicated by black dots, and the dashed lines enclose an area of 4π .

Schematically, when the storage mode is displaced far from the origin of phase space, the dispersive interaction results in two quickly separating trajectories, each corresponding to a different transmon eigenstate. We employ this evolution within a sequence of fast storage displacements intertwined with transmon rotations to engineer an arbitrary conditional displacement in $1.1 \mu\text{s}$, following the unitary evolution $\mathbf{CD}(\beta) = \exp[i(-\text{Re}(\beta)\mathbf{p} + \text{Im}(\beta)\mathbf{q})\frac{\sigma_z}{2}]$ (see Supplementary Figs. 2, 4). This entangling gate can equivalently be viewed as a rotation of the transmon’s Bloch vector around the σ_z axis by an angle that depends on the phase-space distribution of the storage mode. When applied to a transmon initialized on the equator of its Bloch sphere, it leads to $\langle \sigma_x - i\sigma_y \rangle = \langle \mathbf{D}(\beta) \rangle$ (ref. 8). Intuitively, given that the measurement of a displacement by β is a measurement of a quadrature modulo $2\pi/\beta$, the conditional displacement is such that two oscillator quadrature eigenstates separated by $2n\pi/\beta$ induce the same qubit rotation up to an integer number of turns n .

Conditional displacements embedded within a transmon Ramsey sequence enable the measurement of the code stabilizers and, therefore, lay at the heart of the QEC of GKP codes^{22–24}. Conveniently, this sequence is also employed to obtain the expectation value of any displacement operator $\langle \mathbf{D}(\beta) \rangle$ for an arbitrary state of the storage oscillator. This leads to the state characteristic function $C(\beta)$, which is the two-dimensional Fourier transform of the Wigner function^{25,26}. This complex-valued representation fully characterizes an arbitrary state. In our experiment we measure $\text{Re}(C(\beta))$, which contains the information about the symmetric component of the Wigner function, to characterize the generated grid states presented in Figs. 2–4. The imaginary part, $\text{Im}(C(\beta))$, contains information about the antisymmetric component of the Wigner function and is expected to take a uniform null value for the symmetric grid states that we consider. We verify this property at critical points.

Convergence to the GKP code manifold

We now derive a QEC protocol that employs the conditional displacement gate described earlier to protect finite-size grid states. Note that there exists an optimal width of the envelope Δ that results from a trade off: more extended grid states have better resolved peaks and are thus more robust against shifts, but are more sensitive to dissipation. Therefore, our protocol is designed: first, to keep the oscillator state probability distribution peaked in phase space at $q = 0 \text{ mod } 2\pi/|a|$ and $p = 2\pi/|b|$; second, to prevent the overall envelope from drifting or expanding more than necessary. Given our experimental constraints, we work with a finite-size GKP code with envelope width $\Delta \approx 3.2$, chosen

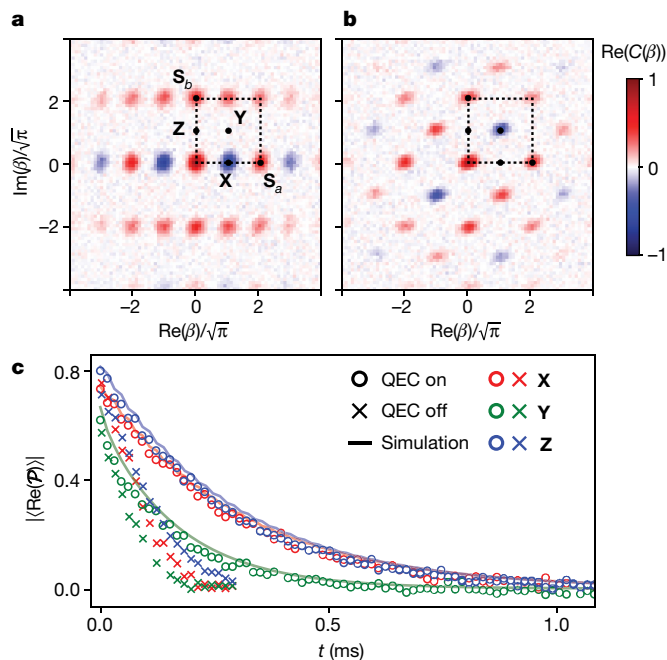


Fig. 3 | Initialization and coherence characterization of the logical qubit in the square encoding. **a**, Characteristic function of $| -X_L \rangle$, prepared in the steady state by applying a feedback **Z** gate conditioned on the outcome +1 of a first single-round $\text{Re}(\mathbf{X})$ measurement, before heralding a higher-fidelity state on the outcome -1 of a second identical measurement. **b**, The same procedure, for $| -Y_L \rangle$. **c**, After preparing $| -X_L \rangle$, $| -Y_L \rangle$ or $| -Z_L \rangle$, the time decay of the real part of $\mathcal{P} = \mathbf{X}, \mathbf{Y}, \mathbf{Z}$, respectively, is measured while continuously applying the QEC protocol (on) or not (off). The QEC protocol extends the lifetime of the three Bloch vector components to $T_x = T_z = 275 \mu\text{s}$ and $T_y = 160 \mu\text{s}$, and the results are quantitatively reproduced by master-equation simulations (lines).

to maximize the coherence time of the logical qubit (see Supplementary Fig. 9).

From the above discussion, maintaining the phase-space distribution peaked at the grid points involves mapping the stabilizers S_a or S_b onto the ancilla transmon with conditional displacements, and then performing actuating displacements based on transmon measurements. As the measurement of the transmon yields only a binary outcome, these steps are constructed to answer the simple questions of whether the grid has moved up or down (when measuring S_a) and whether it has moved left or right (when measuring S_b). After each measurement, we apply a fixed-length displacement in the direction opposite to that indicated by the answer (see Fig. 1). The combination of the back-action of the measurements and of our feedback sharpens the peaks of the grid states. Similar measurements of small displacement operators and feedback trim the envelope of the grid states to keep it from drifting and expanding (see Supplementary Fig. 10). The repeated action of this basic protocol forms a discrete-time Markovian sequence that leads to an effective dissipative force that pushes the state of the storage oscillator towards the code manifold, as depicted in Fig. 1a. This engineered dissipation counteracts the evolution due to noise, thereby inhibiting logical errors.

Starting from the ground state of the oscillator, we apply this protocol indefinitely, as summarized in Fig. 1b. In Fig. 2a we plot the measured average values of $\text{Re}(S_a)$ and $\text{Re}(S_b)$ after n correction rounds. The stabilizer values increase rapidly to converge to a steady state in about 20 rounds. In addition to this trend, the mean value of each stabilizer oscillates over a period of four rounds by increasing to 0.62 when the peaks are sharpened in the corresponding phase-space quadrature, and then decays to 0.5 over the next three rounds. Beyond this periodic

oscillation, the stabilizers do not evolve over hundreds of rounds (not shown), which indicates that our protocol has entered a steady state. The characterization of this steady state can now reveal whether it corresponds to the desired GKP manifold.

We plot the real part of the characteristic function of the steady state after 200 rounds in Fig. 2b. This state is a maximally mixed state of the logical qubit, as can be seen from the null value of the points corresponding to the three logical Pauli operators. Note that this characteristic function representation is the Fourier conjugate of the theoretical Wigner representation given in Fig. 1a. However, the two are similar for grid states because the Fourier transform of a grid is itself a grid. Our results are quantitatively reproduced by master-equation simulations (lines in Fig. 2a), the parameters of which are all calibrated independently. From these simulations, we estimate that the squeezing of the peaks of the generated grid states oscillates between 7.4 dB and 9.5 dB in the steady state—close to the level required for fault-tolerant quantum computation^{27–29}—and the average photon number oscillates between 8.6 and 10.2.

Logical qubit initialization

Once the oscillator has reached its steady state, it is in the code manifold, and we initialize the logical qubit by replacing one of the QEC rounds with a measurement of \mathbf{X}, \mathbf{Y} or \mathbf{Z} . To measure the logical Pauli operators, we first prepare the transmon in $| +x \rangle$ and then apply the conditional displacement $\mathbf{CD}(\beta)$ with $\beta = a/2, (a + b)/2$ or $b/2$, respectively. After the sequence, $\langle \sigma_x - i\sigma_y \rangle = \langle \mathbf{X} \rangle, \langle \mathbf{Y} \rangle$ or $\langle \mathbf{Z} \rangle$, and a subsequent σ_x readout of the transmon with outcome ± 1 heralds the preparation of the approximately orthogonal states $| \pm X_L \rangle, | \pm Y_L \rangle$ or $| \pm Z_L \rangle$ up to a re-centring displacement (see Supplementary Fig. 9).

However, because \mathbf{X}, \mathbf{Y} or \mathbf{Z} differ from the Pauli operators of the finitely squeezed code that we consider, the sequence described above results in a readout of the logical qubit with non-unit fidelity and in an imperfect initialization. Fortunately, when this sequence is followed by a few QEC rounds projecting the generated state back onto the code manifold, this readout is non-demolition for the target logical state and can be repeated to increase its fidelity (see Supplementary Information). In Fig. 3a (Fig. 3b) we show the characteristic function of the storage state obtained when two \mathbf{X} (\mathbf{Y}) measurements, separated by four QEC rounds, yield the same outcome. The expectation values of the Pauli operators in these two cases are $\langle \text{Re}(\mathbf{X}) \rangle = -0.8$ and $\langle \text{Re}(\mathbf{Y}) \rangle = -0.63$, respectively. We emphasize here that these values do not reflect the preparation fidelity to the finitely squeezed logical states $| -X_L \rangle$ and $| -Y_L \rangle$, and the prepared state is as close (within experimental uncertainties) to the target state as allowed by the imperfect code correction (see Supplementary Information). The same methods are applied to prepare eigenstates of other Pauli operators (data not shown) and can be modified to prepare non-Clifford states (see Supplementary Fig. 13). In particular, the characteristic function of the $| -Z_L \rangle$ state is the same as that of $| -X_L \rangle$ rotated by 90° (see Supplementary Fig. 7).

Coherence of the error-corrected logical qubit

To test the error-correction performance of our protocol, we prepare one of the logical states $| -X_L \rangle, | -Y_L \rangle$ or $| -Z_L \rangle$, and compare the decay of the mean value of the real part of the corresponding operator $\mathcal{P} = \mathbf{X}, \mathbf{Y}, \mathbf{Z}$ in time when performing QEC (open circles in Fig. 3b) and when not (crosses in Fig. 3b). In all three cases, our protocol extends the coherence of the logical qubit. We extract the coherence times of the error-corrected qubit $T_x = T_z = 275 \mu\text{s}$ and $T_y = 160 \mu\text{s}$. The shorter coherence time of the \mathbf{Y} Pauli operator, also visible in the uncorrected case, is expected, because the distance in phase space from the probability peaks of the $| +Y_L \rangle$ state to those of the $| -Y_L \rangle$ state is shorter by $\sqrt{2}$ than in the case of $| \pm X_L \rangle$ and $| \pm Z_L \rangle$. Therefore, diffusive shifts in phase space induced by photon dissipation cause more flips of the \mathbf{Y} component

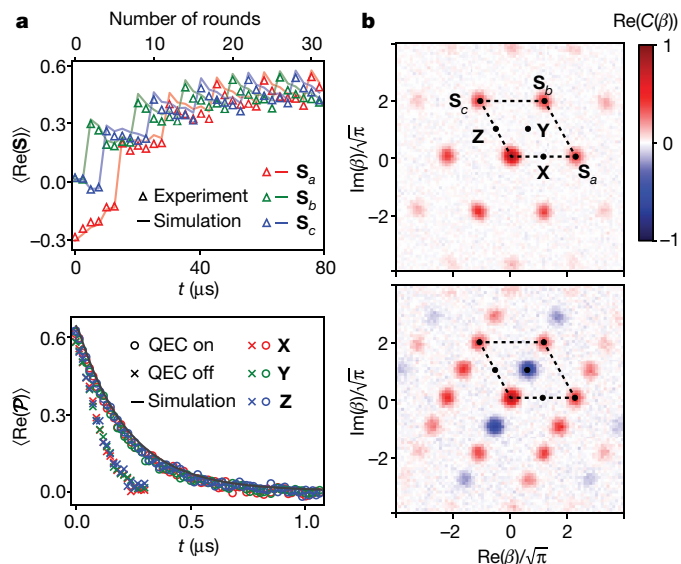


Fig. 4 | Convergence to the code manifold, state preparation and coherence in the hexagonal code. **a**, The grid-state peaks and envelope are sequentially sharpened and trimmed along three directions. When turning on our protocol from the ground state of the oscillator, the real part of the expectation values of the stabilizers oscillates every six rounds and increases to rapidly reach a steady state. **b**, After 200 rounds, the oscillator state is a fully mixed logical state that reveals the code structure (top). An eigenstate of a Pauli operator, such as $|-Y_L\rangle$ (bottom), can be prepared by a single-round measurement of $\text{Re}(Y)$, followed by a feedback displacement. **c**, Owing to the code symmetry, the decay of the logical Bloch vector is isotropic. An exponential fit (black line) indicates a lifetime of $205 \mu\text{s}$, enhanced by QEC.

of the logical qubit Bloch vector. Master-equation simulations reproduce these results quantitatively.

Hexagonal code

We executed a variant of the square code of Fig. 1 known as the hexagonal code, in which the decay times of all three Pauli operators are equal by symmetry. In general, a two-dimensional grid-state code is defined as the common eigenspace of any two commuting stabilizers $S_a = \mathbf{D}(a)$ and $S_b = \mathbf{D}(b)$, as long as $\text{Im}(a^*b) = 4\pi$. Geometrically, this condition implies that the magnitude of the cross-product of the two vectors representing these stabilizers corresponds to an area of 4π (see Figs. 2b, 4b, Supplementary Fig. 12). In the hexagonal GKP code², we have $b = a \exp(i\frac{\pi}{3})$, which respects the above area condition for $a = \sqrt{(8\pi/\sqrt{3})}$. The Pauli operators correspond to displacements of equal length, $\mathbf{X} = \mathbf{D}(a/2)$, $\mathbf{Y} = \mathbf{D}(b/2)$ and $\mathbf{Z} = \mathbf{D}(c/2)$ with $c = a \exp(i\frac{2\pi}{3})$. For symmetry reasons, we also define a third stabilizer, $S_c = \mathbf{Z}^2 = \mathbf{D}(c)$, that commutes with the two others.

We perform QEC on this code by adapting the protocol described in section ‘Convergence to the GKP code manifold’. Here, measurement of the three hexagonal stabilizers, followed by small corrective feedback displacements, sharpens the peaks along three different directions. These steps are interleaved with the measurement of three short displacement operators, which trim the envelope. When applying this protocol on the storage mode initialized in the ground state, the mean values of the stabilizers oscillate every six rounds as each of these displacement operators is measured in turn, and rapidly converge to a stationary regime in which their values oscillate between 0.4 and 0.55 (see Fig. 4a). We measure the real part of the characteristic function of the fully mixed logical state reached after 200 rounds, which reveals the hexagonal structure of the code (Fig. 4b). Again, master-equation simulations reproduce these results quantitatively and indicate that

the generated grid states are characterized by the same squeezing for the peaks as in the square encoding (between 7.5 dB and 9.5 dB in the steady state). Note that the temporary negative value of $\text{Re}(S_a)$ registered at short times originates from the programming of the feedback algorithm on the fast FPGA (field-programmable gate array) board: the oscillator state gets shifted at the beginning of the sequence, which is included in the simulations.

We prepare the logical qubit in an eigenstate of each Pauli operator with a single-round measurement of $\text{Re}(X)$, $\text{Re}(Y)$ or $\text{Re}(Z)$. In Fig. 4b we show the measured characteristic function of the $|-Y_L\rangle$ state. We note that the characteristic functions of $|-X_L\rangle$ and $|-Z_L\rangle$ are equal to that of $|-Y_L\rangle$ but rotated by $\pm 60^\circ$ (see Supplementary Fig. 8). Finally, we characterize the coherence of the error-corrected logical qubit by measuring the decay of the Pauli operator mean values in time. As expected, the decoherence of the logical qubit is now isotropic and considerably extended compared to the uncorrected case, with coherence times of $T_x = T_y = T_z = 205 \mu\text{s}$.

Logical errors and outlook

The coherence of the logical qubit is limited by two factors. First, the duration of the error-correction rounds, despite being a factor of 100 shorter than the storage-mode single-photon lifetime, is not negligible. The transmon readout and its processing using the FPGA accounts for about half of this duration, and the conditional displacement gate accounts for the other half. Although the gate speed is limited in this implementation, alternative implementations could result in faster gates³⁰. The second factor limiting the coherence of the logical qubit is transmon errors. Among these, σ_x errors (phase-flips) commute with the storage–transmon interaction Hamiltonian and thus do not propagate to the logical qubit (see Supplementary Information). On the other hand, the σ_x and σ_y transmon errors (bit-flips), as well as excitations to the higher excited states of the transmon (see Supplementary Fig. 6), propagate to the logical qubit as they lead to random displacements of the storage mode. Simulations indicate that bit-flips of the transmon and the finite correction rate each account for about half of the error rate of the logical qubit (see Supplementary Table 2).

The coherence of the logical qubit could be further improved by replacing the transmon with a noise-biased ancillary qubit^{31–33} and by using a superconducting cavity with a larger quality factor²⁰. This multipronged effort at improving the GKP code using superconducting circuits will be particularly rewarding because fault-tolerant single- and multi-qubit Clifford gates can be implemented in a straightforward way^{2,34}, and such logical qubits can be embedded in further layers of protection^{27–29,35}.

Online content

Any methods, additional references, Nature Research reporting summaries, source data, extended data, supplementary information, acknowledgements, peer review information; details of author contributions and competing interests; and statements of data and code availability are available at <https://doi.org/10.1038/s41586-020-2603-3>.

- Shor, P. Fault-tolerant quantum computation. In *Proc. 37th Conf. Foundations of Computer Science* 56–65 (IEEE, 1996).
- Gottesman, D., Kitaev, A. & Preskill, J. Encoding a qubit in an oscillator. *Phys. Rev. A* **64**, 012310 (2001).
- Travaglione, B. & Milburn, G. J. Preparing encoded states in an oscillator. *Phys. Rev. A* **66**, 052322 (2002).
- Pirandola, S., Mancini, S., Vitali, D. & Tombesi, P. Continuous variable encoding by ponderomotive interaction. *Eur. Phys. J. D* **37**, 283–290 (2006).
- Vasconcelos, H. M., Sanz, L. & Glancy, S. All-optical generation of states for “encoding a qubit in an oscillator”. *Opt. Lett.* **35**, 3261–3263 (2010).
- Terhal, B. & Weigand, D. Encoding a qubit into a cavity mode in circuit QED using phase estimation. *Phys. Rev. A* **93**, 012315 (2016).
- Motes, K. R., Baragiola, B. Q., Gilchrist, A. & Menicucci, N. C. Encoding qubits into oscillators with atomic ensembles and squeezed light. *Phys. Rev. A* **95**, 053819 (2017).

8. Flühmann, C., Negnevitsky, V., Marinelli, M. & Home, J. P. Sequential modular position and momentum measurements of a trapped ion mechanical oscillator. *Phys. Rev. X* **8**, 021001 (2018).
9. Flühmann, C. et al. Encoding a qubit in a trapped-ion mechanical oscillator. *Nature* **566**, 513–517 (2019).
10. Waldherr, G. et al. Quantum error correction in a solid-state hybrid spin register. *Nature* **506**, 204–207 (2014).
11. Kelly, J. et al. State preservation by repetitive error detection in a superconducting quantum circuit. *Nature* **519**, 66–69 (2015).
12. Cramer, J. et al. Repeated quantum error correction on a continuously encoded qubit by real-time feedback. *Nat. Commun.* **7**, 11526 (2016).
13. Ofek, N. et al. Extending the lifetime of a quantum bit with error correction in superconducting circuits. *Nature* **536**, 441–445 (2016).
14. Hu, L. et al. Quantum error correction and universal gate set operation on a binomial bosonic logical qubit. *Nat. Phys.* **15**, 503–508 (2019).
15. Albert, V. V. et al. Performance and structure of single-mode bosonic codes. *Phys. Rev. A* **97**, 032346 (2018).
16. Noh, K., Albert, V. V. & Jiang, L. Quantum capacity bounds of gaussian thermal loss channels and achievable rates with Gottesman–Kitaev–Preskill codes. *IEEE Trans. Inf. Theory* **65**, 2563–2582 (2019).
17. Cahill, K. E. & Glauber, R. J. Ordered expansions in boson amplitude operators. *Phys. Rev.* **177**, 1857–1881 (1969).
18. Aharonov, Y., Pendleton, H. & Petersen, A. Modular variables in quantum theory. *Int. J. Theor. Phys.* **2**, 213–230 (1969).
19. Popescu, S. Dynamical quantum non-locality. *Nat. Phys.* **6**, 151–153 (2010).
20. Reagor, M. et al. Quantum memory with millisecond coherence in circuit QED. *Phys. Rev. B* **94**, 014506 (2016).
21. Wallraff, A. et al. Strong coupling of a single photon to a superconducting qubit using circuit quantum electrodynamics. *Nature* **431**, 162–167 (2004).
22. Kitaev, A. Y. Quantum measurements and the abelian stabilizer problem. Preprint at <https://arxiv.org/abs/quant-ph/9511026> (1995).
23. Svore, K. M., Hastings, M. B. & Freedman, M. Faster phase estimation. *Quant. Inf. Comp.* **14**, 306–328 (2013).
24. Weigand, D. J. & Terhal, B. M. Generating grid states from Schrödinger-cat states without postselection. *Phys. Rev. A* **97**, 022341 (2018).
25. Haroche, S. & Raimond, J.-M. *Exploring the Quantum* (Oxford Univ. Press, 2006).
26. Walls, D. F. & Milburn, G. J. *Quantum Optics* (Springer Science & Business Media, 2007).
27. Glancy, S. & Knill, E. Error analysis for encoding a qubit in an oscillator. *Phys. Rev. A* **73**, 012325 (2006).
28. Fukui, K., Tomita, A., Okamoto, A. & Fujii, K. High-threshold fault-tolerant quantum computation with analog quantum error correction. *Phys. Rev. X* **8**, 021054 (2018).
29. Vuillot, C., Asasi, H., Wang, Y., Pryadko, L. P. & Terhal, B. M. Quantum error correction with the toric Gottesman–Kitaev–Preskill code. *Phys. Rev. A* **99**, 032344 (2019).
30. Touzard, S. et al. Gated conditional displacement readout of superconducting qubits. *Phys. Rev. Lett.* **122**, 080502 (2019).
31. Puri, S. et al. Stabilized cat in driven nonlinear cavity: a fault-tolerant error syndrome detector. *Phys. Rev. X* **9**, 041009 (2019).
32. Grimm, A. et al. The Kerr-cat qubit: stabilization, readout, and gates. *Nature* **584**, 205–209 (2020).
33. Shi, Y., Chamberland, C. & Cross, A. W. Fault-tolerant preparation of approximate GKP states. Preprint at <https://arxiv.org/abs/1905.00903> (2019).
34. Gao, Y. Y. et al. Programmable interference between two microwave quantum memories. *Phys. Rev. X* **8**, 021073 (2018).
35. Baragiola, B. Q., Pantaleoni, G., Alexander, R. N., Karanjai, A. & Menicucci, N. C. All-Gaussian universality and fault tolerance with the Gottesman–Kitaev–Preskill code. Preprint at <https://arxiv.org/abs/1903.00012> (2019).

Publisher's note Springer Nature remains neutral with regard to jurisdictional claims in published maps and institutional affiliations.

© The Author(s), under exclusive licence to Springer Nature Limited 2020

Data availability

The experimental data and numerical simulations presented here are available from the corresponding authors upon request.

Acknowledgements We thank C. Flühmann, J. Home, S. Girvin, L. Jiang and K. Noh for discussions and M. Rooks for fabrication assistance. M.M. thanks the Yale Quantum Institute for hosting him while he was collaborating on this project. The use of facilities was supported by YINQE and the Yale SEAS cleanroom. This research was supported by ARO under grant number W911NF-18-1-0212 and ARO grant number W911NF-16-1-0349.

Author contributions P.C.-I., A.E. and S.T. designed and performed the experiment and analysed the data. E.Z.-G. N.E.F., V.V.S., P.R., S.S., R.J.S. and L.F. contributed to the experimental

apparatus, and S.P. and M.M. provided theoretical support. M.H.D. supervised the project. P.C.-I., A.E., S.T. and M.H.D. wrote the manuscript. All authors provided suggestions for the experiment, discussed the results and contributed to the manuscript.

Competing interests L.F., R.J.S. and M.H.D. are founders of QCI. L.F. and R.J.S. are shareholders of QCI. All authors, except A.E. and E.Z.G., are inventors of patents (USA, Japan and Singapore) related to the subject.

Additional information

Supplementary information is available for this paper at <https://doi.org/10.1038/s41586-020-2603-3>.

Correspondence and requests for materials should be addressed to P.C.-I., S.T. or M.H.D.

Peer review information *Nature* thanks Barbara Terhal and the other, anonymous, reviewer(s) for their contribution to the peer review of this work.

Reprints and permissions information is available at <http://www.nature.com/reprints>.